Competing multiferroic phases in monolayer and few-layer NiI$_2$

Nanshu Liu [1,2] Cong Wang,[1,2] Changlin Yan,[1,2] Changsong Xu,[3] Jun Hu,[4,*] Yanning Zhang,[5,†] and Wei Ji [1,2,5,‡]

[1]*Beijing Key Laboratory of Optoelectronic Functional Materials & Micro-Nano Devices, Department of Physics,*
Renmin University of China, Beijing 100872, China
[2]*Key Laboratory of Quantum State Construction and Manipulation (Ministry of Education),*
Renmin University of China, Beijing 100872, China
[3]*Key Laboratory of Computational Physical Sciences (Ministry of Education), Institute of Computational Physical Sciences, State Key*
Laboratory of Surface Physics and Department of Physics, Fudan University, Shanghai 200433, China
[4]*School of Physical Science and Technology, Ningbo University, Ningbo 315211, China*
[5]*Institute of Fundamental and Frontier Sciences, University of Electronic Science and Technology of China, Chengdu 610054, China*

A recent experiment reported type-II multiferroicity in monolayer (ML) NiI$_2$ based on a presumed spiral magnetic configuration (spiral-B), which is, as we found here, under debate in the ML limit. Freestanding ML NiI$_2$ breaks its C_3 symmetry, as it prefers a striped antiferromagnetic order (AABB-AFM) along with an intralayer antiferroelectric (AFE) order. However, substrate confinement may preserve the C_3 symmetry and/or apply tensile strain to the ML. This leads to another spiral magnetic order (spiral$-$IV^X), while bilayer shows a different order (spiral$-$V^X) and spiral-B dominates in thicker layers. Thus, three multiferroic phases, namely, spiral-B+FE, spiral$-$IV^X + FE, spiral$-$V^X + FE, and an antimultiferroic AABB-AFM+AFE one, show layer thickness dependence and geometry-dependent dominance, ascribed to competition among thickness-dependent Kitaev, biquadratic, and Heisenberg spin-exchange interactions and single-ion magnetic anisotropy. Our theoretical results clarify the debate on the multiferroicity of ML NiI$_2$ and shed light on the role of layer stacking induced changes in noncollinear spin-exchange interactions and magnetic anisotropy in thickness-dependent magnetism.

Magnetoelectric (ME) effects enable the manipulation of magnetic (electric) properties using electric (magnetic) fields, which is of interest in terms of both fundamental physics and potential spintronic applications [1,2]. ME manipulations can be achieved by multiferroic materials exhibiting magnetic and electric orders [3]. Usually, the electric polarization of a type-II multiferroic material is induced by a magnetic order spontaneously through the inverse Dzyaloshinskii-Moriya (DM) interaction [4–7]. However, the identification of type-II multiferroics in atomically thin van der Waals (vdW) monolayers (MLs) is still under debate. NiI$_2$ is a highly promising candidate for ML multiferroicity. Its bulk form undergoes two successive magnetic phase transitions [8,9] from a paramagnetic (PM) phase to an interlayer antiferromagnetic (AFM) phase at $T_{N1} = 76$ K and then to a spiral magnetic phase below $T_{N2} = 59.5$ K [8]. The AFM to spiral transition is accompanied by breaks of both rotational and inversion symmetries, which results in electric polarization through the inverse DM interaction. This effect is reflected in second-harmonic generation (SHG) [10] and birefringence signals [11].

Monolayer NiI$_2$ on an hBN substrate was recently shown to exhibit multiferroicity under 20 K as its enhanced SHG signal strength [11], ascribed to a broken inversion symmetry of either magnetic or geometric (electrical) origin. However,

the magnetic configuration of ML NiI$_2$ below 20 K remains an open issue and previous density functional theory (DFT) predictions are under debate among ferromagnetic (FM) [12–14], helimagnetic [15,16], and AFM [17] configurations. Although not conclusive, they are indeed different from the bulk ground state. If the SHG enhancement originates from the magnetic contribution, it cannot guarantee the formation of additional electric polarization below 20 K [11]. This concern about the claimed multiferroicity was reinforced by the fact that no SHG enhancement was observable in ML NiI$_2$ on a SiO$_2$ substrate [10]. Therefore, the assertion of multiferroic ML NiI$_2$ requires further verification beyond the SHG measurement [11], which raises the question of whether type-II multiferroicity persists in the ML limit.

In this work, we examine the evolution of the magnetic ground state and electric polarization of NiI$_2$ from the bulk to the ML using DFT calculations. We suggest a tentative layer-dependent magnetic phase diagram that illustrates the competition among, at least, four magnetic phases, with three spiral ones (one collinear) being (anti-) ferroelectric and induced by the inverse DM interaction. The magnetic ground state of the ML highly depends on the in-plane geometry to stabilize the competing spiral$-$IV^X (q_{IV}^X) and AABB-AFM configurations under different strains. We additionally demonstrate that these phase changes are driven by the competition among layer thickness and local geometry dependent (non-) collinear Kitaev, biquadratic, and isotropic Heisenberg spin-exchange interactions and single-ion anisotropy. We also construct NiI$_2$/hBN and NiI$_2$/SiO$_2$ heterostructures to

*hujun2@nbu.edu.cn
†yanningz@uestc.edu.cn
‡wji@ruc.edu.cn

consistently explain the SHG signal of ML NiI$_2$ over 20 K obtained by two pioneering experiments [10,11].

The spin-exchange coupling parameters were extracted based on the following Hamiltonian [18],

$$
\begin{aligned}
H = -\frac{1}{2} & \left[\sum_{i,j;x,y,z} J_{ij} \boldsymbol{S}_i \cdot \boldsymbol{S}_j + \sum_{i,j;x,y,z} J_{ij}^{\perp} \boldsymbol{S}_i \cdot \boldsymbol{S}_j \right. \\
& + \sum_{i,j;\alpha,\beta(\gamma)} \left(\lambda_\alpha S_i^\alpha S_j^\alpha + \lambda_\beta S_i^\beta S_j^\beta + \lambda_\gamma S_i^\gamma S_j^\gamma \right) \\
& \left. + \sum_{i,j} B(\boldsymbol{S}_i \cdot \boldsymbol{S}_j)^2 + 2\sum_{i;x,y,z} A_z S_i^2 \right] \\
= -\frac{1}{2} & \left[\sum_{i,j} J_{ij} \boldsymbol{S}_i \cdot \boldsymbol{S}_j + \sum_{i,j} J_{ij}^{\perp} \boldsymbol{S}_i \cdot \boldsymbol{S}_j \right. \\
& \left. + \sum_{i,j} \left(K_{ij}^\gamma S_i^\gamma S_j^\gamma \right) + \sum_{i,j} B(\boldsymbol{S}_i \cdot \boldsymbol{S}_j)^2 + 2\sum_i A_z S_z^2 \right],
\end{aligned}
$$

where A_z represents the single-ion anisotropy, J_{ij} and $J_{ij}^{\perp}$ are the intra- and interlayer isotropic Heisenberg exchange parameters, B and K_{ij}^γ are the biquadratic and collinear Kitaev interaction parameters [19]. We followed the procedures used in our previous calculations [20,21] and have included the details in Appendix A.

Bulk NiI$_2$ crystal has a rhombohedral structure in space group $R\bar{3}m$ at room temperature [Fig. 1(a)], comprising triangularly arranged Ni^{2+} cations ($3d^8$, $S=1$) and coordinating I anions. We used a $1 \times \sqrt{3} \times 1$ supercell to more clearly show magnetic configurations in Fig. 1(e). The calculated lattice constants $a = 3.926\,\text{Å}$, $b = 6.790\,\text{Å}$, and $c = 19.744\,\text{Å}$ of the bulk NiI$_2$ crystal in the experimentally observed spiral order (spiral-B), consistent with the experimental values of $a = 3.919\,\text{Å}$, $b = 6.765\,\text{Å}$, and $c = 19.635\,\text{Å}$ [22]. Spiral-B exhibits a propagation vector $q_B = (0, 0.138, 1.457)$ [Figs. 1(c) and 1(d)] below $T_{N2} = 59.5$ K [11,22]. Note that in the coordinates defined in the literature [11,22], $q_B = (0.138, 0, 1.457)$. Our DFT calculations reproduced this magnetic order suggested in experiments [10,11] and obtained by a spin Hamiltonian [23] in which spiral-B exhibits the lowest energy compared to the five collinear magnetic configurations (Fig. 6 in Appendix B) and 55 other spiral configurations with different q values [Figs. 1(e) and 1(f)]. The spiral-B ground state is robust regardless of the preservation of the C_3 symmetry (Table I), consideration of spin-orbit coupling (SOC) (Fig. 7), and choice of on-site Coulomb interaction (U_{eff}) values (Fig. 8). We are thus confident of the reliability of our results for ML or few-layer NiI$_2$.

The magnetism of ML and few-layer NiI$_2$ is more complicated than bulk NiI$_2$ and difficult to capture by a spin Hamiltonian. We considered 25 collinear and 71 noncollinear magnetic orders using the supercell model and a 10×10 q mesh for the generalized Bloch theorem (GBT) model to explore the layer-dependent magnetic ground states. We focus on the geometries showing (ML-C3) and not showing (ML-NC3) the C_3 symmetry for the ML because the geometric symmetry is more easily modulated by the substrate [24–26].
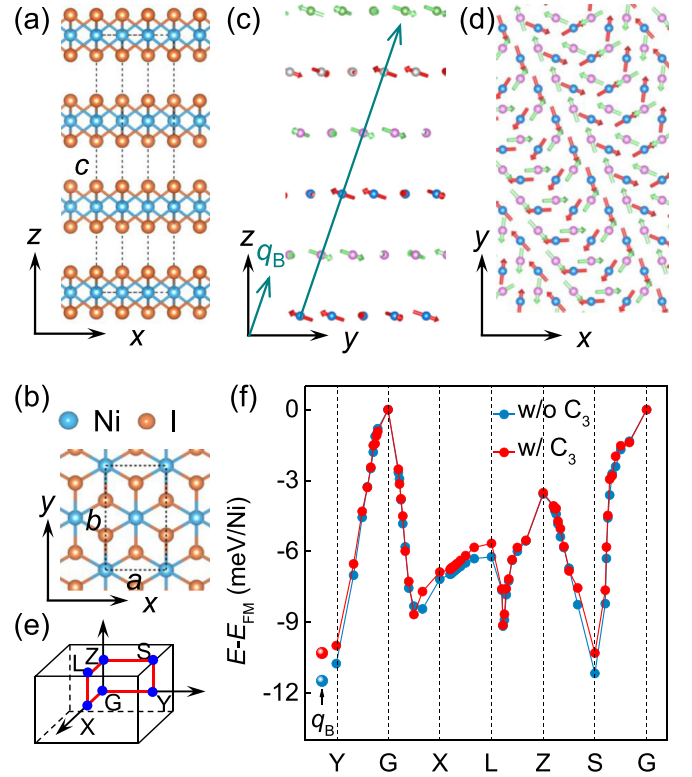

FIG. 1. Side (a) and top (b) views of the atomic structure of bulk NiI$_2$. Schematics of spiral-B in side (c) and top (d) views. Only two Ni layers were plotted in (d) to more clearly show the magnetic moments. (e) q path considered in the first Brillouin zone of a $1 \times \sqrt{3} \times 1$ supercell. (f) Relative energies of all considered spiral orders with (red) and without (blue) preserved C_3 structural symmetry.

For thicker layers, up to four layers (4L), we concentrate on constraint-free geometries as the substrate constraint rapidly relaxes in thicker layers [27].

Figure 2(a) (Fig. 9 in Appendix C) (plots an energy map (profile) for the q mesh (differently sized supercells) of ML-C3 NiI$_2$, where the C_3 symmetry is preserved under constraint. In the following, all energy comparisons were based on the results by constructing supercells including SOC. Both plots indicate a unique spiral configuration [spiral-IV^X, upper inset in Fig. 2(b)], the magnetic moments of which align in the Ni-I plane and follow the propagating vector $q_{\text{IV}}^X = (0.250, 0, 0)$ [across each $4 \times \sqrt{3}$ supercell, Figs. 10(a) and 10(b)], consistent with a recently spin-polarized scanning tunneling microscopy (SP-STM) observation [30], and the same as a previous work but with magnetic moments rotating in the yz plane [31]. Spiral-IV^X shares the same propagation direction with the spiral order discussed in Ref. [11] (spiral-VIII^X) where the propagating period is twice that of spiral-IV^X, namely, eight unit cells (Fig. 11). Spiral-IV^X is, at least, 0.16 meV/Ni more stable than the other spiral orders listed in Table II [e.g., spiral-V^Y, spiral-VII^Y, and spiral-B; see Fig. 2(c)] and a collinear AABB-AFM order [lower inset in Fig. 2(b)], while other configurations (Figs. 12 and 13) are even less stable than the above-mentioned five. Spiral-IV^X is also more stable by at least 0.81 to 1.75 meV/Ni than the two
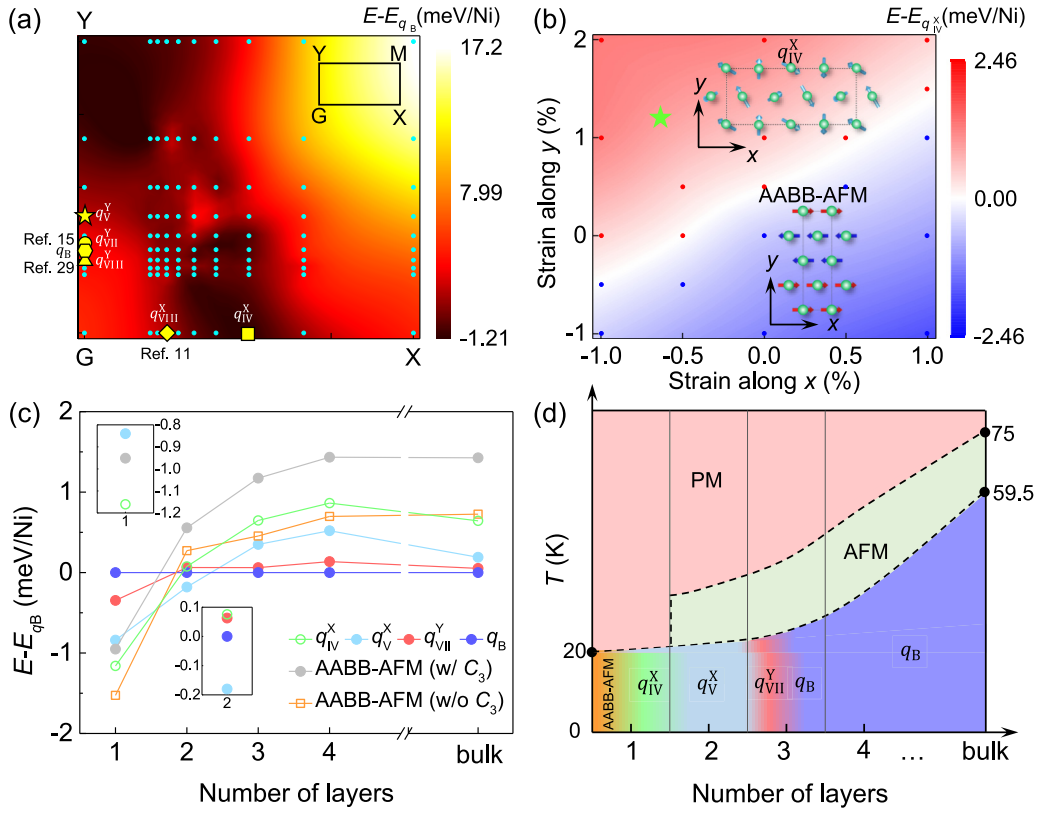
FIG. 2. (a) Energy difference mapping between spin-spiral and spiral-B orders for ML-C3. Inset: q path in the first Brillouin zone of a $1 \times \sqrt{3}$ supercell. The spiral vectors in bulk NiI_2 (q_B), spiral$-IV^X$ (q_{IV}^X), spiral$-V^Y$ (q_V^Y), spiral$-VIII^X$ (q_{VIII}^X) from Ref. [11], spiral$-VII^Y$ (q_{VII}^Y) from Ref. [15], and spiral$-VIII^Y$ (q_{VIII}^Y) from Ref. [28] are indicated by yellow polygons. (b) Energy difference between AABB-AFM and spiral$-IV^X$ versus epitaxial strains along the x and y directions for ML-NC3. Insets: top views of spiral$-IV^X$ and AABB-AFM orders. The green star denotes the strain values of ML NiI_2 being applied from an hBN substrate. The original data were represented by colored dots in (a), (b). (c) Layer-dependent energy difference between the spin-spiral and spiral-B orders for both structures. Insets: zoomed-in energies for ML and 2L NiI_2. (d) Schematic magnetic phase diagrams for different NiI_2 layers versus temperature, with PM and AFM representing paramagnetic and interlayer AFM states, respectively. The transition temperatures were taken from an experimental work [29].

recently theoretically suggested [15,28] and one experimentally observed [32] spiral orders.

In the constraint-free case, the AABB-AFM structure breaks the C_3 symmetry (ML-NC3), which is more stable than spiral$-IV^X$ by 0.35 meV/Ni [Table II and Fig. 2(c)]. This suggests that external strain plays a role in tuning their relative stability. As shown in a phase diagram in Fig. 2(b), spiral$-IV^X$ is substantially stabilized under in-plane compressive strain along the x direction and/or tensile strain along the y direction [red zone in Fig. 2(b)]. Order spiral$-IV^X$ is, at least, 0.12 meV/Ni more stable than spiral$-V^Y$ and spiral$-VII^Y$ in the whole considered strain range, while order AABB-AFM becomes even more stable than order spiral$-IV^X$ in certain strain regions (Fig. 14 in Appendix D). Thus the magnetic ground state was compared between spiral$-IV^X$ and AABB-AFM orders for simplicity.

For constraint-free 2L NiI_2, the AABB-AFM order becomes less stable compared to those spiral orders. A unique spiral order, spiral$-V^X$ (q_V^X), emerges and is 0.26 meV/Ni more stable than spiral$-IV^X$. Spiral$-V^X$ also propagates in the x direction, following vector $q_V^X = (0.20, 0, 0)$, almost degenerated with the order observed in the SP-STM

experiment [30], where a spiral order exhibits $5.01a$, deviating by $7°$ from the x direction. Spiral$-V^X$ is more stable than spiral$-VII^Y$ (q_{VII}^Y) and spiral-B by 0.24 and 0.18 meV/Ni, respectively [Table III in Appendix E, Fig. 2(c)], nearly energetically undistinguishable. Here, spiral$-VII^Y$ propagates along the y direction across a 1×7 supercell and represents the in-plane projection of spiral-B, indicating that the interlayer noncollinear spin-spin interactions are rather weak compared to their in-plane counterparts. Breakdown or preservation of the C_3 symmetry does not essentially change the relative stability of these spiral orders (Table III).

Spiral$-VII^Y$ and spiral-B are still energetically undistinguishable in trilayer (3L), but over 0.35 meV/Ni more stable than spiral$-IV^X$ and spiral$-V^X$ (Table IV). In 4L and thicker layers, the interlayer spin-spin interactions play a more crucial role as spiral-B becomes the ground state by at least 0.14 meV/Ni (Table V). These results depict a layer-dependent competition of one collinear and four spiral orders within four layers, as schematically summarized in the magnetic phase diagram [Fig. 2(d)].

We examined the impact of U_{eff} and the functional on relative energies of those competing configurations. The U_{eff}

values up to 5.4 eV do not affect their relative stability [Fig. 15(a) in Appendix F] and are already larger than the values used in the literature [33] and obtained by a linear response method [34]. Their stability was also verified using the Perdew-Burke-Ernzerhof (PBE), PBE-D3, revised PBE, and HSE06 hybrid functionals considering SOC [Fig. 15(b)], despite numerical discrepancies between the results obtained from HSE06 and other functionals.

Orders spiral$-$IV^X, spiral$-$V^X, and spiral-B (spiral$-$VII^Y) induce electric polarization through the inverse DM interaction, represented by $P||e \times q$, where e denotes the rotational axis of the spiral spins [35]. In Fig. 3(a), the clockwise-rotating spins propagating along the x direction in the q_{IV}^X generate an in-plane electric polarization in the y direction (P_y), perpendicular to bulk in the experiment [8]. A switchable polarization vector characterizes an FE material rather than an electret. Figure 3(b) illustrates a likely intermediate configuration in a switching process of rotating spins propagating from the $+x$ (q_{IV}^X) to the $-x$ direction [$-q_{IV}^X$, Fig. 3(c)]. The change in the propagating direction switches the electric polarization from $+y$ [Fig. 3(a)] to $-y$ [Fig. 3(c)], surmounting an energy barrier of ~ 6 meV in ML-C3 NiI$_2$ [Fig. 16(a) in Appendix G], which is comparable to that of FE ML SnSe (3.76 meV) [36] but smaller than FE ML Bi (43 meV) [37]. The electric polarizations for spiral$-$VII^Y and spiral-B are in the x direction (P_x) for their propagating directions along the y direction. In Fig. 3(d), the bulk value of 0.90 pC/m (for spiral-B) gradually drops to 0.24 pC/m in ML-C3 (spiral$-$IV^X), comparable to the values for ML FeOCl (~ 0.39 pC/m) [38] and ML Hf$_2$VC$_2$F$_2$ (0.29 pC/m) [39].

However, the AABB-AFM order in ML-NC3 eliminates the total electric polarization and exhibits intralayer antiferroelectricity for the shrunk lattice along the y axis accompanied

TABLE I. Relative energies (ΔE) of bulk NiI$_2$ in various collinear and NCL magnetic configurations (shown in Fig. 6). The energy of the spiral-B [$q_B = (0, 0.138, 1.457)$] order was set to the reference zero. The values in parentheses represent the cases without C_3 symmetry. Lattice $m \times n$ indicates the number of supercells in the a and b directions. Spiral-B is the magnetic ground state of bulk NiI$_2$.

Lattice	Mag. config.	ΔE (meV/Ni)
$4 \times \sqrt{3}$	$q_{IV}^X = (0.250, 0, 0)$	0.64 (0.64)
$5 \times \sqrt{3}$	$q_V^X = (0.200, 0, 0)$	0.19
1×4	$q_{IV}^Y = (0, 0.250, 0)$	1.91
1×5	$q_V^Y = (0, 0.200, 0)$	0.31
1×6	$q_{VI}^Y = (0, 0.167, 0)$	0.21
1×7	FM	10.82
	$q_{VII}^Y = (0, 0.143, 0)$	0.05
	$q_B = (0, 0.138, 1.457)$	0
1×8	$q_{VIII}^Y = (0, 0.125, 0)$	0.48
$1 \times 2\sqrt{3}$	AABB-AABB-AABB-AFM	1.43 (0.73)
	AABB-ABBA-BBAA-AFM	1.57
	ABAB-ABAB-ABAB-AFM	18.33
	ABAB-BABA-ABAB-AFM	23.17

TABLE II. Relative energies ΔE of ML NiI$_2$ with the C_3 symmetry limitation (ML-C3) in different collinear and NCL magnetic configurations. The energy of q_B order was set to the reference zero. The values in parentheses represent the cases without C_3 symmetry (ML-NC3). The magnetic ground state of ML-C3 is spiral$-$IV^X (q_{IV}^X), while that for ML-NC3 is AABB-AFM order.

Lattice	Mag. config.	ΔE (meV/Ni)
$2 \times \sqrt{3}$	$q_{II}^X = (0.500, 0, 0)$	7.80 (7.34)
$3 \times \sqrt{3}$	$q_{IV}^X = (0.333, 0, 0)$	1.19 (0.90)
$4 \times \sqrt{3}$	$q_{IV}^X = (0.250, 0, 0)$	-1.16 (-1.33)
$5 \times \sqrt{3}$	$q_V^X = (0.200, 0, 0)$	-0.84 (-0.93)
$6 \times \sqrt{3}$	$q_{VI}^X = (0.167, 0, 0)$	0.01 (-0.05)
$7 \times \sqrt{3}$	$q_{VII}^X = (0.143, 0, 0)$	0.54 (0.51)
$8 \times \sqrt{3}$	$q_{VIII}^X = (0.125, 0, 0)$	1.44 (1.42)
1×2	$q_{II}^Y = (0, 0.500, 0)$	23.67 (19.50)
1×3	$q_{III}^Y = (0, 0.333, 0)$	7.91 (8.04)
1×4	$q_{IV}^Y = (0, 0.250, 0)$	-0.37 (0.38)
1×5	$q_V^Y = (0, 0.200, 0)$	-1.00 (-1.04)
1×6	$q_{VI}^Y = (0, 0.167, 0)$	-0.72 (-0.77)
1×7	FM	4.61 (5.37)
	$q_{VII}^Y = (0, 0.143, 0)$	-0.35 (-0.38)
	$q_B = (0, 0.138, 1.457)$	0 (-0.15)
1×8	$q_{VIII}^Y = (0, 0.125, 0)$	0.59 (0.55)
3×2	NCL	15.23
3×3	NCL	8.35
$\sqrt{3} \times \sqrt{3}$	NCL	8.82
$2\sqrt{3} \times \sqrt{3}$	NCL	4.10
$1 \times 2\sqrt{3}$	AABB-AFM	-0.95 (-1.68)
	ABAB-AFM	19.46 (24.17)

by Ni atom relaxation [Table VI and Fig. 3(e)]. The Ni atoms in the same AFM stripe move oppositely by 0.004 Å in the $\pm y$ directions [Fig. 3(f)], yielding a dipole moment of ± 1.5 pC/m [Fig. 3(g)]. The switching barrier [Fig. 16(b)] between the two AFE configurations is ~ 6 meV, comparable to the FE barrier of ML spiral$-$IV^X.

In short, few-layer NiI$_2$ exhibits at least four competing multiferroic phases: the newly found spiral$-$IV^X + FE, spiral$-$V^X + FE, and AABB-AFM + AFE states and the previously known spiral-B + FE state. Thus, ML NiI$_2$ is indeed a type-II multiferroic material, but with tunable multiferroicity between AFM + AFE and spiral + FE by the in-plane geometry. This helps explain the seemingly contradictory experimental results [10,11], where ML NiI$_2$ was supported on SiO$_2$ [10] and hBN [11] substrates, suggesting the substrate may play a role in affecting their in-plane geometry.

The ML NiI$_2$ was epitaxially grown on an hBN substrate [11], while the structural details of ML-NiI$_2$ on the hBN substrate remain unknown in experiments. We thus theoretically considered the ML-NiI$_2$/hBN interface exhibiting the smallest lattice mismatch and lowest total energy [27]. We used an ML NiI$_2$ $10 \times 4\sqrt{3}$ / ML hBN $9\sqrt{3} \times 11 - R30°$ rectangular supercell, in which the hBN substrate applies a compressive
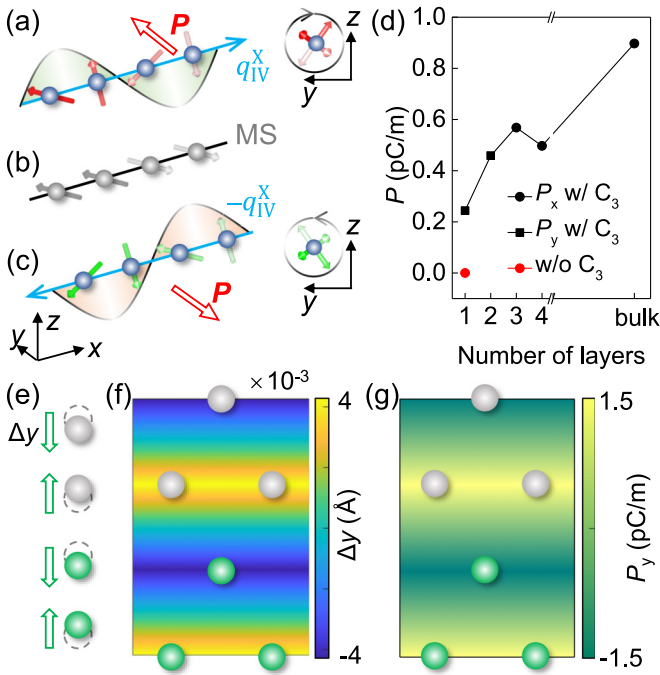
FIG. 3. Schematic plots for a spin canting process from (a) a clockwise propagation in spiral$-$IV^X (q_{IV}^X) to (c) a counterclockwise one ($-q_{IV}^X$) through (b) a likely metastable state (MS). The (counter-) clockwise spin spiral generates an in-plane electric polarization (anti-) parallel to the y direction. (d) Theoretical electric polarization versus the number of NiI$_2$ layers. (e), (f) Displacement of Ni atoms in AABB-AFM along the y direction in ML-NC3. (g) Electric polarization induced by displacements of Ni atoms in the AABB-AFM state.

FIG. 4. (a) Side view of the optimized geometrical structure of a NiI$_2$ ML deposited on an amorphous SiO$_2$ substrate. (b) Line profiles along the z direction of charge variations for the NiI$_2$/$h-$BN and NiI$_2$/SiO$_2$ heterostructures. The z coordinates of the interfacial I atoms were set to zero. Two-dimensional (2D) mappings of spatial variation of vertical distances between lower I atoms and (c) top-layer B or N atoms of the hBN substrate and (d) surface O atoms of the SiO$_2$ substrate.

strain of -0.6% along the x direction and a tensile strain of $\sim 1.3\%$ along the y to ML NiI$_2$. This supercell is 1.43 and 2.48 meV/Ni more stable than the two configurations (Fig. 17 in Appendix H) exhibiting the second and third smallest interfacial strains, which are in the tensile strain region. The Ni layer [Fig. 18(a)] and the two I sublayers (Fig. 19) exhibit out of plane corrugations varying up to 0.06 Å. Nonuniform in-plane strains further break the inversion symmetry in the x [Fig. 18(c)] and y [Fig. 18(d)] directions. Moreover, explicit interfacial charge transfer from the BN layer to the interfacial I layer leads to out of plane electric polarization [Figs. 18(e) and 18(f)]. Therefore, ML NiI$_2$ on hBN simultaneously breaks its structural inversion symmetry, corresponding to the observable SHG signals above 20 K in Ref. [11].

These strong modifications from hBN to ML NiI$_2$ indicate their strong interactions. NiI$_2$ is, most likely, prone to maintain its C_3 symmetry on hBN due to the confinement from the C_3 symmetrized hBN. For ML-C3, spiral$-$IV^X is preferred over AABB-AFM and is further stabilized under biaxial compressive strains and electron doping [Figs. 14(b) and 20 in Appendix I]. Thus the SHG signal could be further enhanced by the additional in-plane electric polarization induced by the noncollinear spiral$-$IV^X order formed below 20 K [11]. However, the amorphous SiO$_2$ substrate is a well-saturated substrate that exhibits weak interactions with its supporting MLs [40]. The validity of this statement for ML NiI$_2$ was
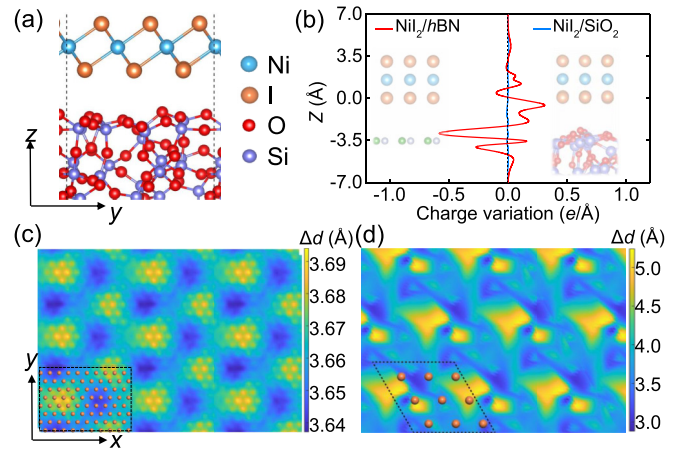
supported by our theoretical comparison of the NiI$_2$/SiO$_2$ and NiI$_2$/hBN interfaces (Fig. 4 and Appendix J), in which the NiI$_2$/SiO$_2$ interface shows negligible interfacial charge variations [Fig. 4(b)] and larger interfacial distance variations [Figs. 4(c) and 4(d)]. The SiO$_2$ substrate thus interacts more weakly with NiI$_2$, leading the NiI$_2$ overlayer closer to its free-standing form. Therefore, ML NiI$_2$ placed on amorphous SiO$_2$ most likely favors the collinear AABB-AFM order and thus shows no temperature-dependent SHG enhancement [10].

The remaining issue is why ML and few-layer NiI$_2$ host at least four competing states. We plotted the layer dependence of various magnetic interactions (Fig. 5). Parallel coupled Heisenberg J_1 [black in Fig. 5(a)] nearly maintains its bulk value of 3.22 meV down to 3L and then rapidly increases to 3.55 meV in 2L and 3.89 meV in ML [Fig. 5(b)]. Antiparallel coupled J_3 [blue in Fig. 5(a)] exhibits almost the opposite trend [Fig. 5(b)]. Their competition could lead to noncollinear spin-spiral states if $|J_1/J_3| < 4$ [41]. The DFT revealed that $|J_1/J_3|$ ranges from 0.92 to 1.26 for NiI$_2$ layers [Fig. 5(c)] and fits this criterion well, while the strongest (weakest) frustration occurs in bulk (ML) where the ratio reaches its minimum (maximum) among all considered layer thicknesses.

Two-site anisotropy J_{yz} characterizes the preference of the direction of magnetic moments canting from the xy plane to the z axis [28]. The bulk NiI$_2$ exhibits $J_{yz} = 1.90$ meV and the largest J_{yz}/J_1 ratio of 0.59 [Fig. 5(d)], indicating the preferred out of plane (OOP) orientations of the magnetic moments in thicker layers, consistent with their OOP easy axes [Figs. 21(b) and 21(c) in Appendix K)] and the in-plane one in ML [Fig. 21(e)]. Single-ion anisotropy A_z, favoring the moments oriented in the z axis, follows the same trend and reaches its maximum positive value of 1.60 meV [Fig. 5(d)] in bulk NiI$_2$. A considerably large Kitaev interaction $K = 2.44$ meV [see Fig. 5(d)] confines magnetic moments in the α-β plane [Fig. 1(c)], which leads to spiral-B being more
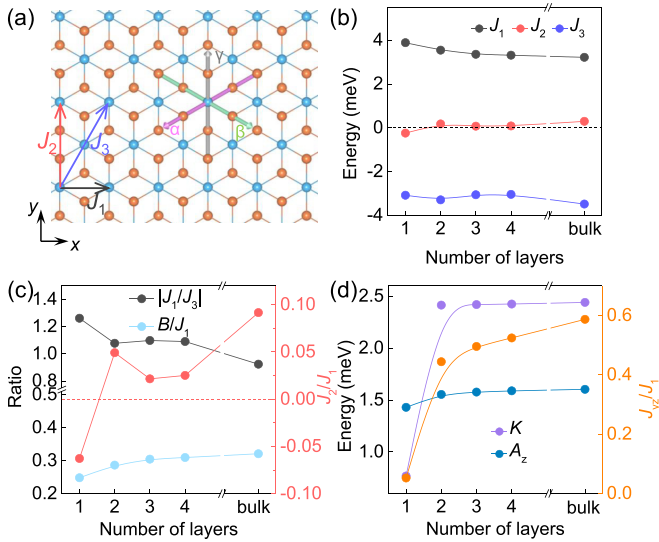
FIG. 5. (a) Schematic illustration of the Kitaev basis $\{\alpha\beta\gamma\}$ (magenta, green, and gray arrows) and the intralayer isotropic first to third nearest-neighbor Heisenberg spin-exchange parameters J_1 to J_3. (b) Layer-dependent evolution of J_1, J_2, and J_3. (c) Ratios of $|J_1/J_3|$, J_2/J_1, and B/J_1. (d) Noncollinear J_{yz} over J_1 (J_{yz}/J_1), Kitaev K, and single-ion anisotropy A_z.

stable than its xy-plane projection spiral$-\mathrm{VII}^Y$. The moments in spiral-B are slightly off the α-β plane owing to competition between K and A_z.

For layers thinning from bulk down to 4L–2L, the ratio between the competing FM J_2 and J_1 (J_2/J_1) decreases from approximately 0.03 (4L) to 0.02 (3L) and then increases to 0.05 (2L) [Fig. 5(c)], which results in the emergence of a spatially smaller spiral order (spiral$-\mathrm{V}^X$) in 2L. However, configurations spiral-B and spiral$-\mathrm{VII}^Y$ are energetically indistinguishable in 2L, because of multiple competing interactions such as the slightly reduced A_z, and nearly unchanged $|J_1/J_3|$ ratio and K. The second interlayer nearest-neighbor exchange parameter ($J_2^\perp$) is AFM and dominates for bulk to 2L (Tables VII and VIII in Appendix L), resulting in interlayer AFM couplings between NiI$_2$ layers.

In the ML limit, the ratio J_2/J_1 changes to be negative with a larger value of -0.06 [Fig. 5(c)], which, together with parallel coupled biquadratic magnetic dipole interaction B, leads to the competing AABB-AFM and spiral$-\mathrm{IV}^X$ configurations. The ratios of B and J_2 over J_1 determine the preferred order; that is, the larger the ratio(s) are, the more favored is the AABB-AFM configuration [23]. This is verified by the comparison between the ML-NC3 and ML-C3 structures and the enlarged ratios in the reinforced AABB-AFM state under tensile strain (Tables VII and VIII).

In summary, we exploited four multiferroic phases of NiI$_2$ from bulk to the ML limit. Their magnetic ground states are spiral-B, spiral$-\mathrm{VII}^Y$, spiral$-\mathrm{V}^X$, spiral$-\mathrm{IV}^X$, and AABB-AFM. Those magnetic spirals induce in-plane electric polarizations through the inverse DM interaction. Thus, ML NiI$_2$ is a type-II multiferroic material with multiferroicity between AABB-AFM+AFE and spiral$-\mathrm{IV}^X$ + FE

tunable by structural details. These fruitful variations arise from competitions among layer-dependent Heisenberg (an-)isotropic exchanges, biquadratic and Kitaev interactions, and single-ion anisotropy. While anisotropic and Kitaev interactions and single-ion anisotropy play a paramount role in the bulk limit [23], the competing Heisenberg exchanges and biquadratic interaction dominate the ground states in the ML limit. Our results highlight the importance of the layer thickness and geometry in exploring the multiferroic properties of vdW layers down to the ML limit, although the properties causing variation in magnetic interactions require further understanding.

APPENDIX A: SUPPLEMENTAL METHODS

Density functional theory (DFT) calculations were performed using the generalized gradient approximation (GGA) for the exchange-correlation potential, the projector augmented wave (PAW) method [42,43], and a plane-wave basis set as implemented in the Vienna *ab initio* simulation package (VASP) [44,45]. A kinetic energy cutoff of 700 (650) eV for the plane waves was used for structural optimization (calculations on the relative energies). A vacuum layer over 20 Å in thickness in the z direction was adopted to eliminate interactions among image layers. The on-site Coulomb interaction was considered with a U value of 4.2 eV and a J value of 0.8 eV for Ni $3d$ orbitals, according to the literature [12,46] and our energy test calculations of a noncollinear (NCL) and four collinear (CL) magnetic configurations (Fig. 6 in Appendix B). Spin-orbit coupling (SOC) was considered in all total energy calculations. We used the ferromagnetic (FM) configuration as a reference for the comparison of the total energies in differently sized supercells. The total energies of the FM configuration only differ by 0.08 meV/Ni, indicating good energy convergence for our calculations. Each spiral magnetic order was modeled using a certain propagation vector q within the first Brillouin zone of a $1 \times \sqrt{3} \times 1$ supercell using the generalized Bloch theorem (GBT) [47]. We also constructed supercells of those spiral orders with lower energies obtained by the GBT along the $Y - G - X$ path in
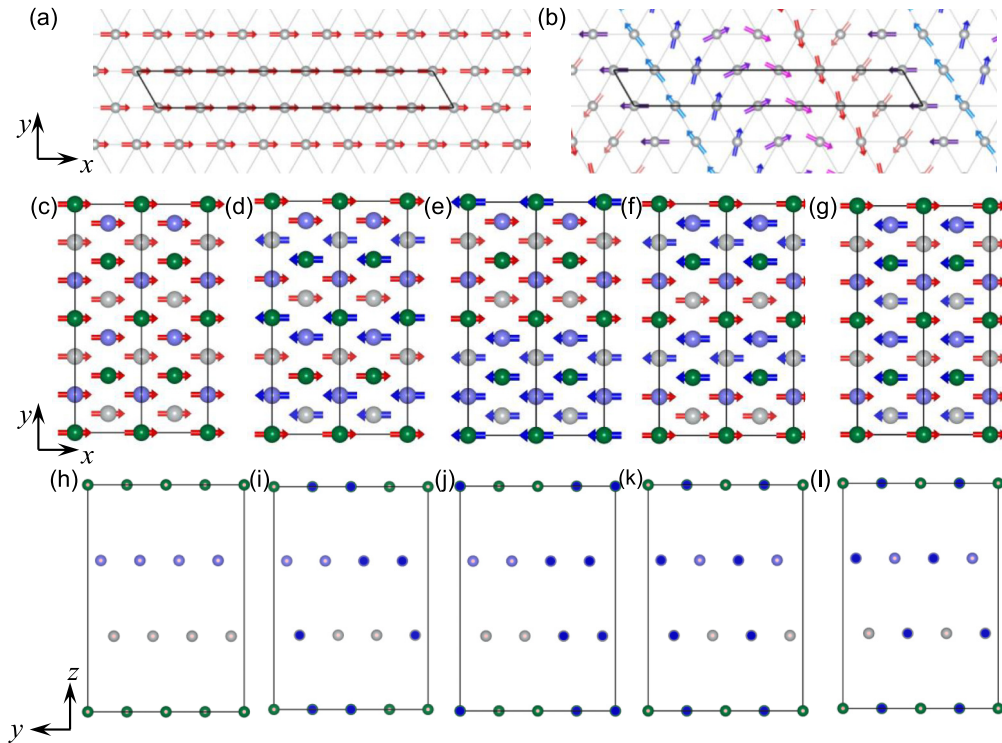
FIG. 6. Schematic models of various collinear and noncollinear (NCL) magnetic configurations for bulk NiI$_2$ considered in this work, including top views of (a) FM and (b) spiral orders in a $7 \times 1 \times 1$ supercell, and (c) FM, (d) AABB-ABBA-AABB-AFM, (e) AABB-AABB-AABB-AFM, (f) ABAB-ABAB-ABAB-AFM, and (g) AABB-BABA-ABAB-AFM orders in a $1 \times 2\sqrt{3} \times 1$ supercell, with magnetic moments along the x direction. The configuration "AABB-ABBA-AABB-AFM" means AABB-AFM, ABBA-AFM, and AABB-AFM magnetic orders in the first, second, and third NiI$_2$ layers, which are labeled by green, gray, and blue balls, respectively. (h)-(l) Side views corresponding to (c)-(g). The black boxes represent different supercells. Directions of magnetic moments are labeled by colored arrows.

the first Brillouin zone for different layers to verify their relative stabilities under consideration of SOC. The Berry phase method [48] was adopted to evaluate the spiral magnetic order induced electric polarization. The FM state, showing no electric polarization, was used as the reference state to show the layer dependence of the electric polarization values. The

transition barrier for monolayer (ML) NiI$_2$ from the in-plane antiferroelectric (AFE) phase of the AABB antiferromagnetic (AFM) order to a nonelectric phase with C_3 symmetry was calculated using the climbing image nudged elastic band (CINEB) method [49]. All atoms, lattice volumes, and shapes
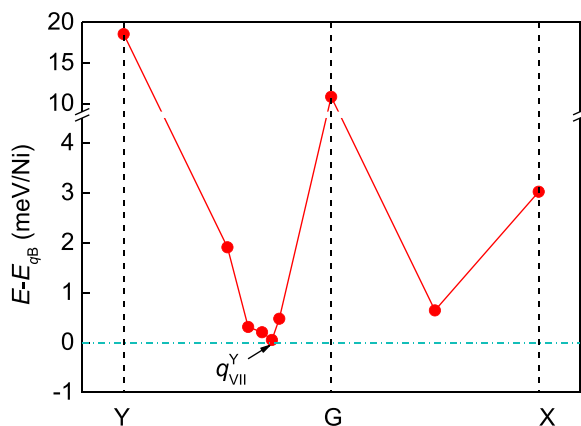

FIG. 7. Energies of various spiral orders along the $Y - G - X$ path in different supercells relative to the total energy of the q_B order (represented by the horizonal dashed cyan line) in bulk NiI$_2$. Spin-orbit coupling was considered in all supercells. The comparable order q_{VII}^Y is labeled, which is the in-plane projection of spiral-B. Spiral-B is the ground state of bulk NiI$_2$.
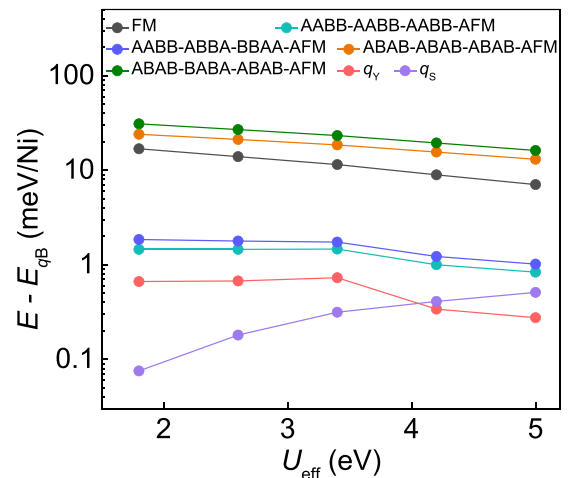

FIG. 8. Effect of different on-site effective Coulomb U values (U_{eff}) on bulk NiI$_2$. Comparison of total energies of different magnetic orders relative to that of q_B as a function of U_{eff} values using the PBE-D3 functional. The two additional spiral orders are $q_Y = (0, 0.5, 0)$ and $q_S = (0, 0.5, 0.5)$. The spiral-B ground state of bulk NiI$_2$ is robust regardless of the choice of U_{eff} values.
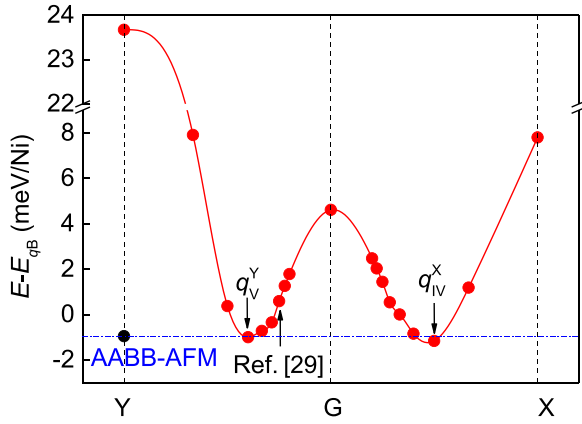
FIG. 9. Comparison of total energies among various spiral orders in different supercells for ML NiI_2 with C_3 symmetry (ML-C3). The energy of the q_B order is set to the reference zero. Spin-orbit coupling is considered in all supercells. The horizontal dashed blue line represents the energy of AABB-AFM order. The energy of ML NiI_2 in Ref. [28] is also indicated.

in each supercell were allowed to relax until the residual force on each atom was less than $0.01\,\text{eV/Å}$. Grimme's semiempirical D3 scheme [50] for dispersion correction was employed to describe the vdW interactions in combination with the Perdew-Burke-Ernzerhof functional (PBE D3) [51]. This combination achieved accuracy comparable to that of the optB86b-vdW functional for describing geometric properties of layered materials [52] at a lower computational cost.

The nearest-neighbor exchange-coupling tensor for Ni–Ni pairs in the xyz basis is

$$J_1^{xyz} = \begin{pmatrix} J_{xx} & 0 & 0 \\ 0 & J_{yy} & J_{yz} \\ 0 & J_{yz} & J_{zz} \end{pmatrix} \tag{A1}$$

If $J_{yz} \neq 0$, adjacent moments will be noncollinearly coupled and lie in a plane off the xy plane [28].

The tensor J_1^{xyz} can be diagonalized in the $\alpha\beta\gamma$ basis shown in Fig. 5(a) in the main text as

$$J_1^{\alpha\beta\gamma} = \begin{pmatrix} \lambda_\alpha & 0 & 0 \\ 0 & \lambda_\beta & 0 \\ 0 & 0 & \lambda_\gamma \end{pmatrix} \tag{A2}$$

Therefore, the nearest-neighbor exchange-coupling Hamiltonian in such a basis can be written as

$$H_1 = -\frac{1}{2} \sum_{i \neq j} \left(\lambda_\alpha S_i^\alpha S_j^\alpha + \lambda_\beta S_i^\beta S_j^\beta + \lambda_\gamma S_i^\gamma S_j^\gamma \right). \tag{A3}$$

For NiI_2, we assume $\lambda_\alpha = \lambda_\beta$. H_1 then can be expressed as

$$H_1 = -\frac{1}{2} \sum_{i \neq j} \left(J S_i \cdot S_j + K S_i^\gamma S_j^\gamma \right), \tag{A4}$$

where $J = (\lambda_\alpha + \lambda_\beta)/2$ is the isotropic nearest-exchange coupling in the $\alpha\beta$ plane and $K = \lambda_\alpha - J$ is the Kitaev anisotropic nearest-exchange coupling parameter.

The calculated J_1^{xyz} of ML NiI_2 with C_3 symmetry is

$$J_1^{xyz} = \begin{pmatrix} 3.67 & 0 & 0 \\ 0 & 4.64 & 0.20 \\ 0 & 0.20 & 3.68 \end{pmatrix}, \tag{A5}$$

and thus

$$J_1^{\alpha\beta\gamma} = \begin{pmatrix} 3.74 & 0 & 0 \\ 0 & 3.74 & 0 \\ 0 & 0 & 4.51 \end{pmatrix} \tag{A6}$$

Therefore, $J_{yz} = 0.20$ meV, $J = 3.74$ meV, and $K = 0.77$ meV. The J_{yz}, J, and K parameters for the other NiI_2 layers can be obtained in a similar way.

APPENDIX B: ENERGY COMPARISONS FOR BULK NiI_2

We considered five collinear (Fig. 6) and 55 NCL [Figs. 1(e) and 1(f)] magnetic configurations. The experimentally observed spiral order (spiral-B) shows the lowest energy among these magnetic orders [Fig. 1(f) and Table I], which is robust regardless of the preservation of the C_3 symmetry
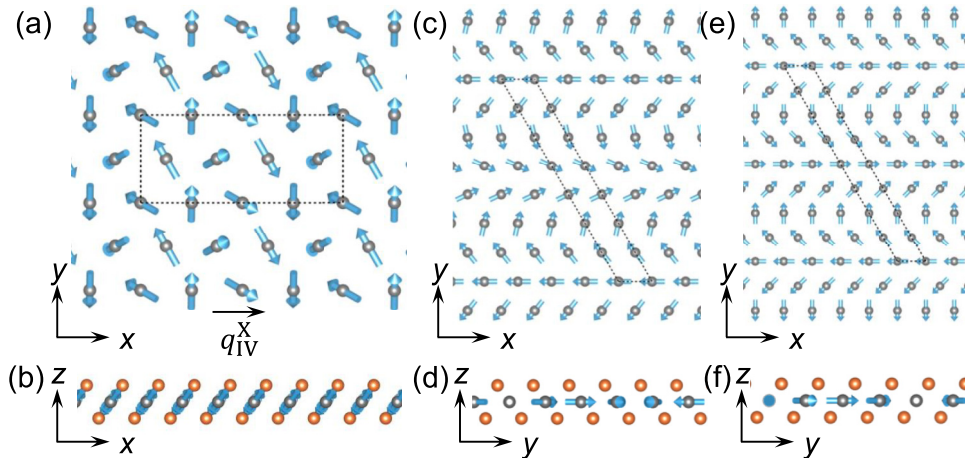

FIG. 10. Schematic plots of spiral orders of ML NiI_2. (a), (b) Top and side views of q_{IV}^X with magnetic moments lying in the $\alpha\beta$ plane [illustrated in Fig. 5(a)]. Spiral orders with propagation vectors along the y direction across (c), (d) a 1×7 and (e), (f) a 1×8 supercell, the magnetic moments of which lie in the xy plane.
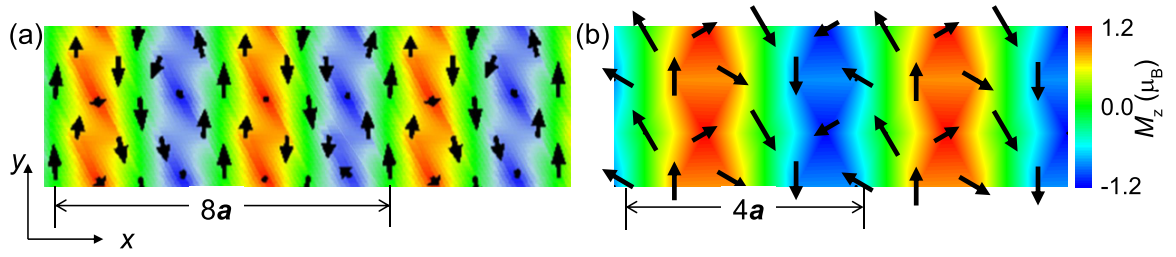
FIG. 11. Magnetic configurations of (a) the spiral order in Fig. 3(c) of Ref. [11] and (b) spiral$-$IV^X. In both figures, black arrows indicate the in-plane components of magnetic moments, while the color maps represent the out of plane components. Their propagating vectors of 8a and 4a were labeled in panels (a), (b), respectively.

[Fig. 1(e)], consideration of SOC (Fig. 7), and choice of on-site Coulomb interaction (Fig. 8) values.

APPENDIX C: TOTAL ENERGY COMPARISONS OF VARIOUS MAGNETIC CONFIGURATIONS IN MONOLAYER NiI₂

For monolayer NiI₂, we considered three collinear and 19 NCL magnetic orders (Figs. 9–13 and Table II) in different supercell sizes (Fig. 9) and a 10×10 q mesh [Fig. 2(a)] for the GBT model to explore the magnetic ground state. Different from the spiral-B in bulk NiI₂, a unique spiral order (spiral$-$IV^X) emerges in ML NiI₂ with C_3 symmetry (ML-C3). The magnetic moments of spiral$-$IV^X align in the Ni-I plane [Fig. 10(b)] and follow a propagating vector $q_{IV}^X = (0.250, 0, 0)$ [across each $4 \times \sqrt{3}$ supercell, Fig. 10(a)]. For the ML NiI₂ without C_3 symmetry (ML-NC3), the AABB-AFM state is more stable than spiral$-$IV^X by 0.35 meV/Ni (Table II). The magnetic ground state of ML NiI₂ is thus dependent on the structural symmetry, indicating that external strains play a role in modulating their relative stability.

APPENDIX D: STRAIN EFFECTS ON THE MAGNETIC GROUND STATE OF ML NiI₂

We also carried out calculations to compare the stability of some competing magnetic configurations under strains. Configurations q_V^Y and q_{VII}^Y were compared with q_{IV}^X and AABB-AFM under x-y epitaxial strains for NiI₂ MLs without the C_3 symmetry (ML-NC3) and the AABB-AFM configuration was also examined under biaxial strains for ML NiI₂ with C_3 symmetry (ML-C3). Figure 14(a) clearly illustrates that either the AABB-AFM or the spiral$-$IV^X order exhibits the best stability among all four considered magnetic orders. In particular, spiral$-$IV^X (red plane) is always more stable than q_V^Y [by 0.12–0.41 meV/Ni, yellow plane in Fig. 14(a)], q_{VII}^Y [by 0.42–1.67 meV/Ni, green plane in Fig. 14(a)] in ML-NC3, and AABB-AFM in ML-C3 [AABB-C3, by 0.14–0.31 meV/Ni, Fig. 14(b)] in the whole considered strain range. In certain strain regions, the AABB-AFM order [blue plane in Fig. 14(a)] becomes more stable than spiral$-$IV^X. Based on these results, we verified the reliability of only comparing the energies of q_{IV}^X and AABB-AFM for competing in the magnetic ground state of ML NiI₂.
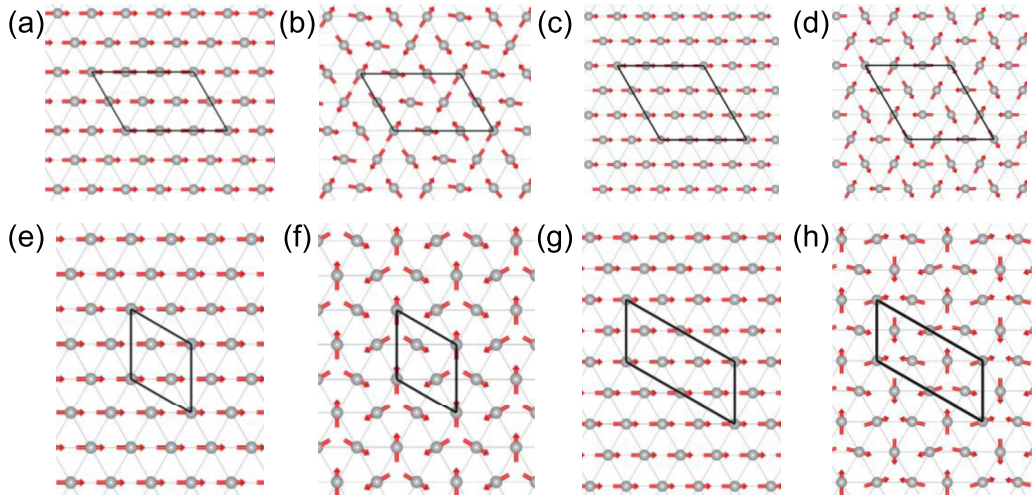

FIG. 12. Schematic plots of collinear and NCL magnetic configurations for ML NiI₂ considered in this work, including (a) FM and (b) NCL in a 3×2 supercell; (c) FM, and (d) NCL in a 3×3 supercell; (e) FM and (f) NCL in a $\sqrt{3} \times \sqrt{3}$ supercell; and (g) FM and (h) NCL in a $2\sqrt{3} \times \sqrt{3}$ supercell. The black boxes represent different supercells. Directions of magnetic moments are indicated by red arrows.
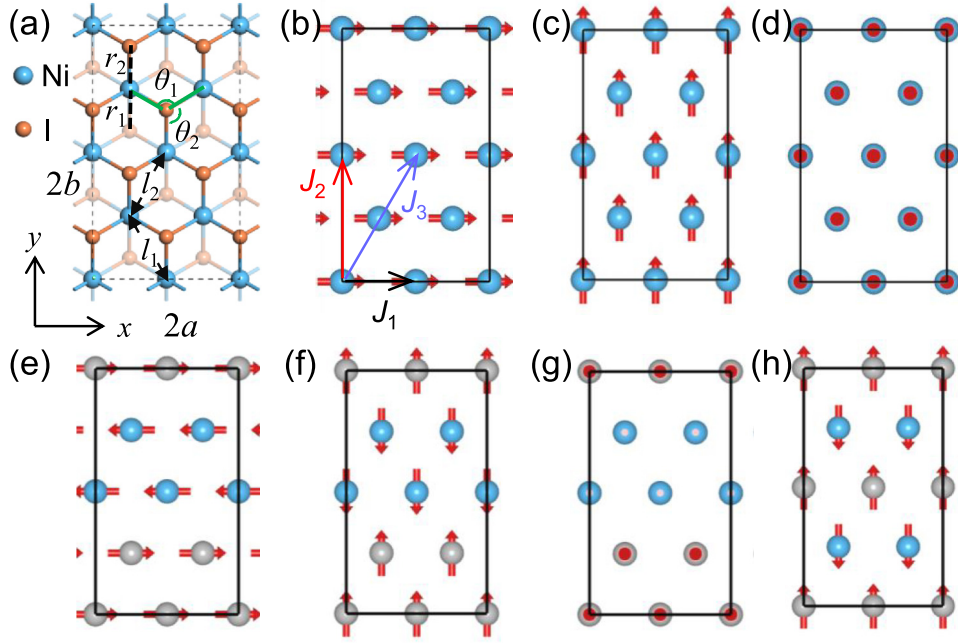
FIG. 13. (a) Structural details of ML NiI$_2$. The black rectangle illustrates the $2 \times 2\sqrt{3}$ supercell. The blue and orange spheres indicate Ni and I atoms, respectively. Several key structural parameters, including r_1, r_2, θ_1, θ_2, l_1, and l_2, are marked. Different collinear magnetic configurations with magnetic moments along the x, y, and z directions are shown, including (b) FM order along the x direction, (c) along the y direction, (d) along the z direction, (e) AABB-AFM order along the x direction, (f) along the y direction, (g) along the z direction, and (h) ABAB-AFM order along the y direction.

APPENDIX E: LAYER-DEPENDENT MAGNETIC GROUND STATES FOR FEW-LAYER NiI$_2$

For constraint-free 2L NiI$_2$, the AABB-AFM order is less stable than other NCL orders (Table III). A unique spiral order, named spiral$-$V^X, emerges and is 0.26 meV/Ni more stable than spiral$-$IV^X. The magnetic moments of spiral$-$V^X propagate along the x direction and across each $5 \times \sqrt{3}$ supercell. Spiral$-$V^X is also more stable than spiral$-$VII^Y

and spiral-B by 0.24 and 0.18 meV/Ni, nearly energetically undistinguishable. The spiral$-$VII^Y is the in-plane projection of spiral-B and propagates along the y direction across a 1×7 supercell. Breakdown or preservation of C_3 symmetry does not change the relative stability of these spiral orders (Table III). For 3L NiI$_2$, spiral$-$VII^Y and spiral-B are still energetically degenerated, but over 0.35 meV/Ni more stable than spiral$-$IV^X and spiral$-$V^X (Table IV). For 4L and
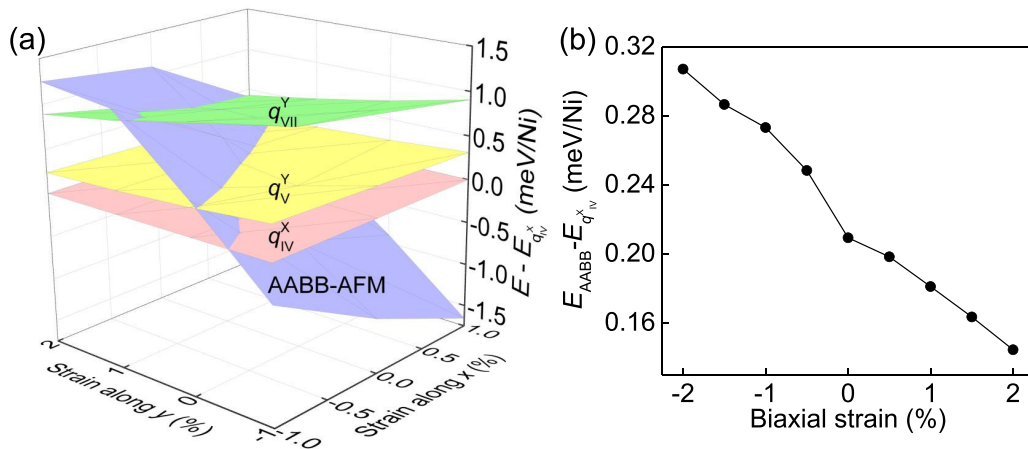

FIG. 14. (a) Relative energies of spiral$-$V^Y (q_V^Y), spiral$-$VII^Y (q_{VII}^Y), and AABB-AFM to that of spiral$-$IV^X (q_{IV}^X) for ML-NC3 under epitaxial strains along the x and y directions. (b) Relative energy of AABB-AFM to q_{IV}^X for ML-C3 as a function of biaxial strains.

TABLE III. Relative energies ΔE of bilayer (2L) NiI_2 with the C_3 symmetry limitation (2L-C3) in different collinear and NCL magnetic configurations. The energy of q_B order was set to reference zero. The values in parentheses represent the cases without C_3 symmetry (2L-NC3).

Lattice	Mag. config.	ΔE (meV/Ni)
$4 \times \sqrt{3}$	$q_{IV}^X = (0.250, 0, 0)$	0.08 (0.02)
$5 \times \sqrt{3}$	$q_V^X = (0.200, 0, 0)$	$-0.18\,(-0.08)$
$6 \times \sqrt{3}$	$q_{VI}^X = (0.167, 0, 0)$	0.27 (0.28)
$7 \times \sqrt{3}$	$q_{VII}^X = (0.143, 0, 0)$	0.42 (0.39)
1×4	$q_{IV}^Y = (0, 0.250, 0)$	1.63
1×5	$q_V^Y = (0, 0.200, 0)$	$-0.03\,(0.14)$
1×6	$q_{VI}^Y = (0, 0.167, 0)$	0.11
1×7	FM	8.11 (8.48)
	$q_{VII}^Y = (0, 0.143, 0)$	0.06 (-0.01)
	$q_B = (0, 0.138, 1.457)$	0 (-0.02)
1×8	$q_{VIII}^Y = (0, 0.125, 0)$	0.64
$1 \times 2\sqrt{3}$	AABB-AABB-AFM	0.56 (0.27)
	AABB-ABBA-AFM	1.03 (0.62)

thicker NiI_2, spiral-B becomes the most stable among various collinear and NCL magnetic configurations (Table V).

APPENDIX F: EFFECTS OF DIFFERENT U_{eff} VALUES AND FUNCTIONALS ON THE MAGNETIC STABILITY OF ML NiI_2

We examined the effect of on-site effect U_{eff} values and functionals on the magnetic ground state of ML NiI_2. As

TABLE IV. Relative energies ΔE of trilayer (3L) NiI_2 with the C_3 symmetry limitation (3L-C3) in different collinear and NCL magnetic configurations. The energy of q_B order was set to reference zero. The values in parentheses represent the cases without C_3 symmetry (3L-NC3).

Lattice	Mag. config.	ΔE (meV/Ni)
$4 \times \sqrt{3}$	$q_{IV}^X = (0.250, 0, 0)$	0.65 (0.90)
$5 \times \sqrt{3}$	$q_V^X = (0.200, 0, 0)$	0.35
$6 \times \sqrt{3}$	$q_{VI}^X = (0.167, 0, 0)$	0.50
1×4	$q_{IV}^Y = (0, 0.250, 0)$	2.19
1×5	$q_V^Y = (0, 0.200, 0)$	0.44
1×6	$q_{VI}^Y = (0, 0.167, 0)$	0.20
1×7	FM	9.44
	$q_{VII}^Y = (0, 0.143, 0)$	0.06
	$q_B = (0, 0.138, 1.457)$	0
1×8	$q_{VIII}^Y = (0, 0.125, 0)$	0.61
$1 \times 2\sqrt{3}$	AABB-AABB-AABB-AFM	1.17 (0.45)
	AABB-ABBA-BBAA-AFM	1.84
	ABAB-ABAB-ABAB-AFM	18.01
	ABAB-BABA-ABAB-AFM	22.76

TABLE V. Relative energies ΔE of four-layer (4L) NiI_2 with the C_3 symmetry limitation (4L-C3) in different collinear and NCL magnetic configurations. The energy of q_B order was set to reference zero. The values in parentheses represent the cases without C_3 symmetry (4L-NC3).

Lattice	Mag. config.	ΔE (meV/Ni)
$4 \times \sqrt{3}$	$q_{IV}^X = (0.250, 0, 0)$	0.86 (0.70)
$5 \times \sqrt{3}$	$q_V^X = (0.200, 0, 0)$	0.52
$6 \times \sqrt{3}$	$q_{VI}^X = (0.167, 0, 0)$	0.57
1×4	$q_{IV}^Y = (0, 0.250, 0)$	2.40
1×5	$q_V^Y = (0, 0.200, 0)$	1.28
1×6	$q_{VI}^Y = (0, 0.167, 0)$	0.30
1×7	FM	10.15
	$q_{VII}^Y = (0, 0.143, 0)$	0.14
	$q_B = (0, 0.138, 1.457)$	0
1×8	$q_{VIII} = (0, 0.125, 0)$	0.64
$1 \times 2\sqrt{3}$	AABB-AABB-AABB-AABB-AFM	1.44 (0.70)
	AABB-AABB-ABBA-ABBA-AFM	1.69
	AABB-ABBA-ABBA-AABB-AFM	1.55
	AABB-AABB-AABB-ABBA-AFM	1.69
	ABBA-ABBA-ABBA-AABB-AFM	1.31

shown in Fig. 15(a), for ML-NC3 (ML-C3), the AABB-AFM (q_{IV}^X) state always shows the lowest energy under different U_{eff} values and functionals (orange squares). The relative stability for these magnetic configurations was also checked using the HSE06 functional [Fig. 15(b)].

APPENDIX G: ELECTRIC PROPERTIES FOR ML NiI_2 WITH AND WITHOUT C_3 SYMMETRY

We used the NEB method to calculate the energy barriers for the spin canting process of ML-C3 from q_{IV}^X to $-q_{IV}^X$ [Fig. 16(a)] and AFE transition of ML-NC3 through a non-electric phase [Fig. 16(b)]. As listed in Table VI, the lattice b shrinks for the AABB-AFM state relative to that of FM order. In the AABB-AFM order, the Ni atoms in the same AFM stripe move oppositely by 0.004 Å in the $\pm y$ directions, yielding a dipole moment of ± 1.5 pC/m [Fig. 3(g)].

APPENDIX H: SUBSTRATE EFFECT ON MAGNETIC GROUND STATE OF ML NiI_2

The relation between lattices of the ML NiI_2 and hBN substrate is yet to be uncovered in experiments. Without such experimental input, we theoretically constructed the super-lattices of their heterostructures using a criterion of optimal lattice mismatching. We adopted the supercell with a lattice of -0.6% along the x direction and 1.3% along the y direction (referred to as Str. 1), and an alternative hexangular supercell [referred to as Str. 2, Fig. 17(a)] and a rectangular one [referred to as Str. 3, Fig. 17(b)], exhibiting the second and the third smallest lattices mismatches, namely, 2.1% along both the x and y directions in Str. 2, and 3.8% along the x directions and -4.0% along the y direction in Str. 3. Please be aware
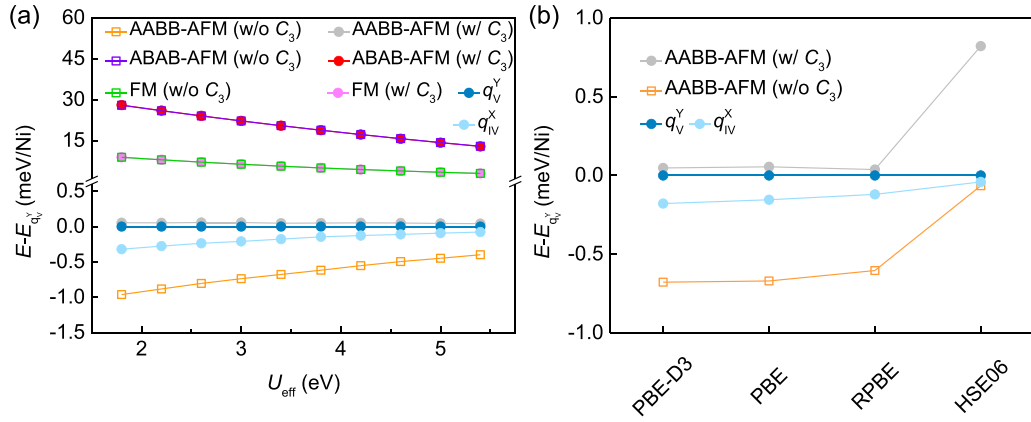
FIG. 15. Total energies of different magnetic orders to that of the spiral$-V^Y$ state were shown as functions of (a) effective U_{eff} values using the PBE-D3 functional and (b) functionals with $U_{eff} = 3.8$ eV. Spin-orbit coupling is considered in the PBE-D3, PBE, and RPBE functionals. U_{eff} is not used for the HSE06 functional calculation.
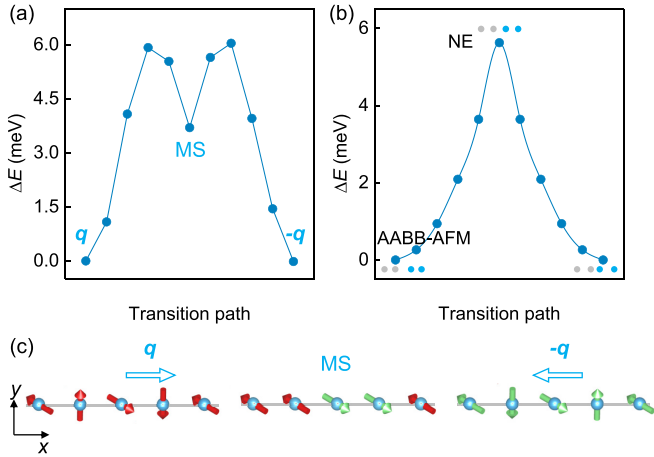

FIG. 16. (a) Calculated energy barrier for the spin canting process of ML NiI$_2$, taking spiral$-$IV^X order [illustrated in Figs. 3(a)–3(c)]. (b) Transition pathway for ML NiI$_2$ between the two AFE phases through a nonelectric (NE) phase. The blue and gray circles represent the Ni atoms in different magnetic stripes. (c) Initial, metastable (MS) and final magnetic configurations for the spin canting process in (a).

that the strains in Str. 2 are in the tensile region, while the $x(y)$ strain in Str. 3 is in the opposite direction of that for Str. 1, namely, tensile (compressive) $x(y)$ strain. Our calculations indicate that Str. 1 is 1.43 and 2.48 meV/Ni more stable than Str. 2 and Str. 3, respectively, given a defined interfacial binding energy $E_b = E_{tot} - E_{hBN} - E\text{NiI}_2$, where E_{tot}, E_{hBN}, and $E\text{NiI}_2$ denote the energies of the heterostructure, hBN, and NiI$_2$, respectively.

In Str. 1, the Ni layer [Fig. 18(a)] and the two I sublayers (Fig. 19) exhibit out of plane corrugations varying up to 0.06 Å. In-plane strains break the inversion symmetry in the x [Fig. 18(c)] and y [Fig. 18(d)] directions. Moreover, explicit interfacial charge transfer from the hBN substrate to the interfacial I layer leads to an out of plane electric polarization [Figs. 18(e) and 18(f)].

APPENDIX I: EFFECT OF ELECTRON DOPING ON THE RELATIVE STABILITY BETWEEN SPIRAL$-$IV^X AND AABB-AFM ORDERS

We considered the effect of electron doping on the relative stability between AABB-AFM and spiral$-$IV^X for both structures. As shown in Fig. 20, for ML-C3, the spiral$-$IV^X is always more stable than the AABB-AFM (red dots), while it is preferred for doping concentration larger than 0.02 e/I for ML-NC3 (black dots). The hBN substrate interacts strongly with ML NiI$_2$; the C_3 symmetry of ML

TABLE VI. Structural details of ML NiI$_2$ in a $2 \times 2\sqrt{3}$ supercell with different magnetic configurations [marked in Fig. 13(a)]. "Sym." represents the space point group symmetry.

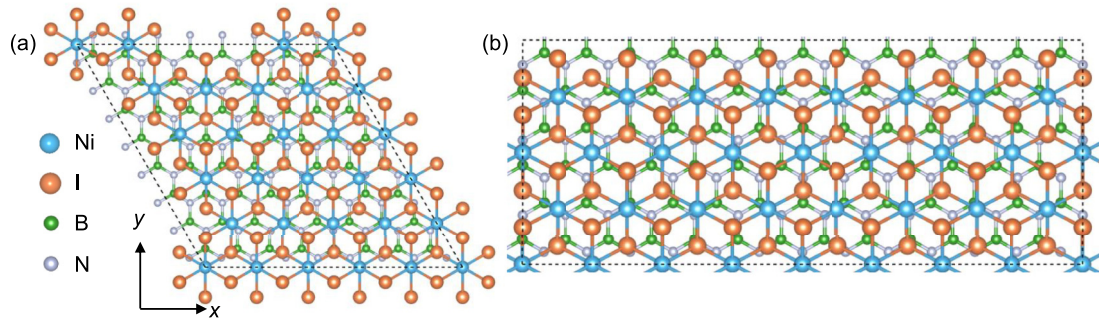| Spin config.	$2a$ (Å)	$2\sqrt{3}b$ (Å)	l_1 (Å)	l_2 (Å)	θ_1 (deg)	θ_2 (deg)	Sym.
FM	7.86	13.61	3.93	3.93	91.21	91.21	$P\bar{3}m1$
AABB-AFM	7.85	13.56	3.91	3.93	90.98	91.15	$P21/m$
ABAB-AFM	7.86	13.61	3.93	3.93	91.18	91.18	$P21/m$
ZZ-AFM	7.87	13.63	3.91	3.93	90.95	91.13	$P2/C$

FIG. 17. Top view of two alternative NiI_2/hBN heterostructures in the tensile strain region, exhibiting lattice mismatches of 2.1% for the x and y directions in (a) and 3.8% along the x direction and -4.0% along the y direction in (b). The hexangular and rectangular supercells are depicted, highlighting the relative arrangement of the layers.

NiI_2 thus is, most likely, maintained on hBN. Moreover, electrons are transferred from hBN to ML NiI_2 [Fig. 18(e)]. The magnetic ground state of ML NiI_2 on hBN is thus the spiral$-IV^X$.

APPENDIX J: COMPARISON OF INTERFACIAL INTERACTIONS FOR NiI_2/hBN AND NiI_2/SiO$_2$ HETEROSTRUCTURES

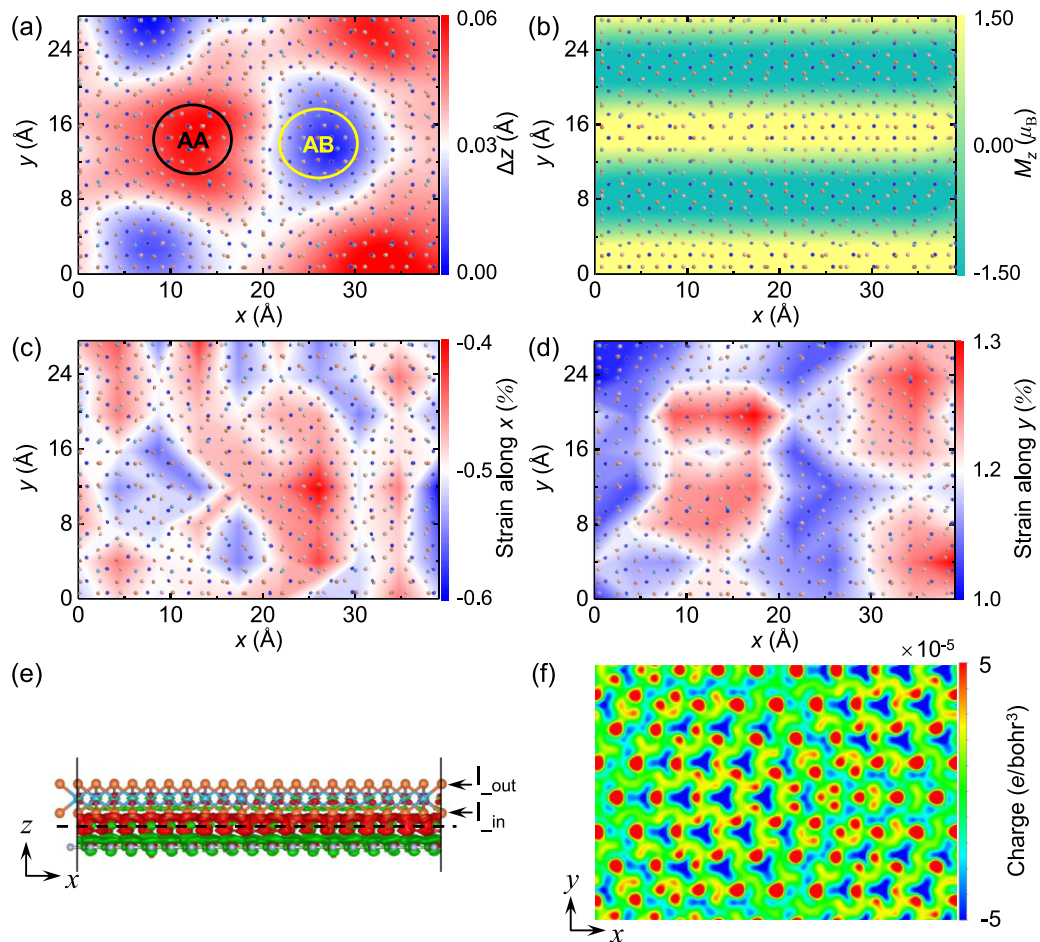To more clearly show the different interfacial interactions for ML NiI_2 on hBN and SiO$_2$ substrates, we performed

FIG. 18. Structure and magnetism of the epitaxial ML NiI_2 on a hBN substrate, including 2D mappings of the variation in (a) the z coordinates and (b) the magnetic moments of Ni atoms in the heterostructure taking the AABB-AFM state, and in-plane strains along the (c) x and (d) y directions. (e) Side view of differential charge density and (f) 2D profile maps along the dashed lines in (e) with an isosurface value of 5×10^{-5} e/bohr^3. The red and green contours in (e), (f) are charge accumulation and depletion, respectively. The lower and upper I atoms of ML NiI_2 on hBN are labeled by I_{in} and I_{out} in (e).
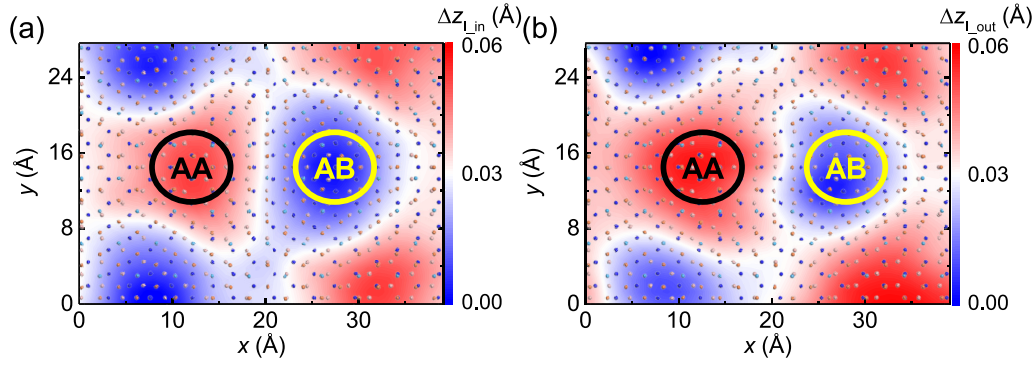
FIG. 19. Two-dimensional mappings of the z-coordinates of the (a) I_{in} and (b) I_{out} atoms [labeled in Fig. 18(e)] of ML NiI$_2$ adsorbed on the hBN substrate. The spatial variations for z coordinates of the I_{in} and I_{out} indicate out of plane inversion symmetry breaking for NiI$_2$ on the hBN substrate.

calculations for ML NiI$_2$ on an amorphous SiO$_2$ substrate. The fully relaxed atomic structure of the NiI$_2$/SiO$_2$ interface is shown in Fig. 4(a). We plotted line profiles along the z direction of interfacial differential charge density (DCD) variations for both NiI$_2$/hBN [red line in Fig. 4(b)] and NiI$_2$/SiO$_2$ [blue line in Fig. 4(b)] interfaces. The NiI$_2$/BN interface exhibits significant charge variations across the interface while that of the NiI$_2$/SiO$_2$ interface is nearly inappreciable, indicating a much weaker interaction of SiO$_2$ to the NiI$_2$ monolayer. The more weakly interacting SiO$_2$ also leads to a less-uniform interfacial structure. As mapped in Fig. 4(c), the SiO$_2$ substrate exhibits a much larger range, namely, from 2.88 to 5.24 Å, for the vertical distance between interfacial I and O atoms. However, the range for the hBN substrate is much narrower, namely, from 3.63 to 3.70 Å, as depicted in Fig. 4(d). The smaller vertical corrugation of the NiI$_2$/hBN interface also gives rise to an average interfacial distance of 3.67 Å, 0.39 Å smaller than that of the NiI$_2$/SiO$_2$ interface (4.06 Å). Therefore, these results indicate that the amorphous SiO$_2$ substrate most likely interacts with the NiI$_2$ ML more weakly than the hBN substrate, which means the SiO$_2$ substrate is less capable of efficiently applying in-plane strain confinements to the NiI$_2$ ML. In other words, the hBN substrate may have a chance to force the NiI$_2$ ML following the C_3 symmetry of the substrate, while the SiO$_2$ substrate, most likely, cannot.

APPENDIX K: EVOLUTION OF LAYER-DEPENDENT MAGNETIC ANISOTROPIC ENERGY (MAE)

We mapped the magnetic anisotropic energies for bulk and few layers NiI$_2$. As shown in Fig. 21, the magnetic moments from ML to bulk NiI$_2$ undergo a spin reorientation from the out-of-plane to in-plane direction.

APPENDIX L: LAYER-DEPENDENT MAGNETIC PARAMETERS

We listed various magnetic coupling parameters in Tables VII and VIII for bulk and few layers NiI$_2$ with and without the C_3 symmetry, respectively. See Tables VII and VIII for more details.
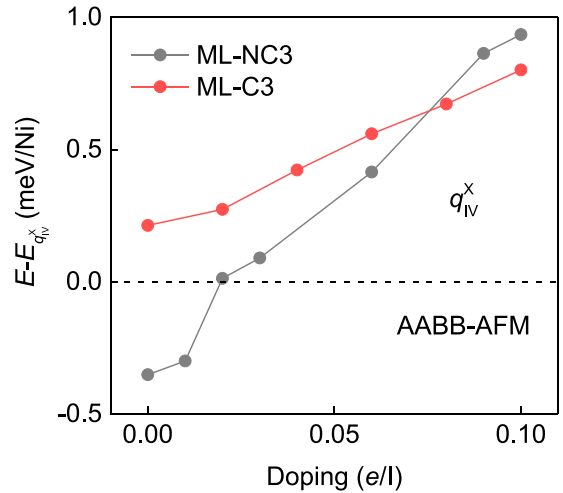

FIG. 20. Energy difference between AABB-AFM and spiral$-IV^X$ orders for ML-NC3 (black) and ML-C3 (red) under different doping concentrations. For ML-NC3, order spiral$-IV^X$ is more stable than AABB-AFM order when doping concentration is larger than 0.02 e/I, while it is always more preferred than AABB-AFM order for ML-C3 under electron doping.
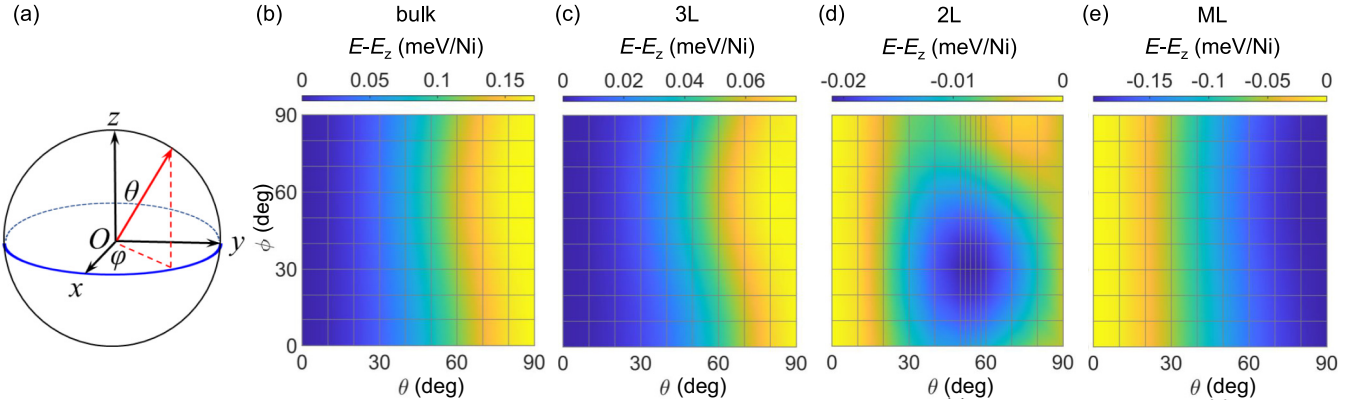
FIG. 21. (a) Illustration of magnetization axes in MAE calculation. Here θ and φ are the angles between the magnetization direction and z and x axes, respectively. Angular dependence energies relative to that of magnetic moment along the z axis for (b) bulk, (c) 3L, (d) 2L, and (e) ML NiI$_2$ taking FM order. From ML to bulk NiI$_2$, magnetic moments undergo a spin reorientation from the in-plane to the out-of-plane direction.

TABLE VII. Isotropic exchange parameters J_1, J_2, and J_3 for the nearest, second nearest, and third nearest Ni atoms, and interlayer isotropic exchange parameters $J_1^\perp$, $J_2^\perp$, and $J_3^\perp$ for the nearest, second nearest, and third nearest Ni atoms, their ratios $|J_1/J_3|$ and J_2/J_1, Kitaev K, single-ion anisotropy A_z, and magnetic dipole interaction over J_1 (B/J_1), and two-site anisotropy over J_1 (J_{yz}/J_1) of NiI$_2$ with C_3 symmetry.

	J_1 (meV)	J_2 (meV)	J_3 (meV)	$J_1^\perp$ (meV)	$J_2^\perp$ (meV)	$J_3^\perp$ (meV)	$|J_1/J_3|$	J_2/J_1	K (meV)	A_z (meV)	B/J_1	J_{yz}/J_1
ML	3.89	−0.25	−3.09	—	—	—	1.26	−0.06	0.77	1.43	0.24	0.05
2L	3.55	0.17	−3.29	0.37	−1.52	−0.28	1.08	0.05	2.41	1.55	0.34	0.44
3L	3.36	0.07	−3.06	0.04	−1.29	−0.23	1.10	0.02	2.42	1.58	0.37	0.49
4L	3.32	0.08	−3.04	0.08	−1.32	−0.24	1.09	0.03	2.42	1.59	0.40	0.52
Bulk	3.22	0.29	−3.48	0.49	−2.05	−0.38	0.92	0.09	2.44	1.60	0.44	0.58

TABLE VIII. Isotropic exchange parameters J_1, J_2, J_3, $J_1^\perp$, $J_2^\perp$, and $J_3^\perp$, and their ratios $|J_1/J_3|$ and J_2/J_1, K, A_z, B/J_1 and J_{yz}/J_1 of NiI$_2$ without C_3 symmetry. "Strained ML" refers to ML-NC3 undergoing a tensile strain of 1.0% along the x direction (Strained ML).

	J_1 (meV)	J_2 (meV)	J_3 (meV)	$J_1^\perp$ (meV)	$J_2^\perp$ (meV)	$J_3^\perp$ (meV)	$|J_1/J_3|$	J_2/J_1	K (meV)	A_z (meV)	B/J_1	J_{yz}/J_1
ML	3.92	−0.26	−3.20	—	—	—	1.22	−0.07	0.77	1.43	0.24	0.05
Strained ML	3.97	−0.34	−3.49	—	—	—	1.23	−0.09	1.73	1.45	0.29	0.25
2L	3.59	0.12	−3.40	0.38	−1.53	−0.28	1.06	0.03	2.41	1.55	0.34	0.44
3L	3.29	0.13	−3.14	0.05	−1.31	−0.24	1.05	0.04	2.42	1.58	0.37	0.49
4L	3.36	0.03	−3.17	0.10	−1.34	−0.25	1.06	0.01	2.42	1.59	0.40	0.52
Bulk	3.27	0.24	−3.61	0.50	−2.05	−0.40	0.91	0.07	2.44	1.60	0.44	0.58

[1] N. A. Spaldin and R. Ramesh, Advances in magnetoelectric multiferroics, Nat. Mater. **18**, 203 (2019).

[2] T. Kimura, T. Goto, H. Shintani, K. Ishizaka, T. Arima, and Y. Tokura, Magnetic control of ferroelectric polarization, Nature (London) **426**, 55 (2003).

[3] N. Terada, D. D. Khalyavin, P. Manuel, F. Orlandi, C. J. Ridley, C. L. Bull, R. Ono, I. Solovyev, T. Naka, D. Prabhakaran, and A. T. Boothroyd, Room-temperature type-II multiferroic phase induced by pressure in cupric oxide, Phys. Rev. Lett. **129**, 217601 (2022).

[4] N. A. Spaldin, Multiferroics: from the cosmically large to the subatomically small, Nat. Rev. Mater. **2**, 17017 (2017).

[5] M. Fiebig, T. Lottermoser, D. Meier, and M. Trassin, The evolution of multiferroics, Nat. Rev. Mater. **1**, 16046 (2016).

[6] S. Dong, H. Xiang, and E. Dagotto, Magnetoelectricity in multiferroics: a theoretical perspective, Natl. Sci. Rev. **6**, 629 (2019).

[7] S. Dong, J.-M. Liu, S.-W. Cheong, and Z. Ren, Multiferroic materials and magnetoelectric physics: symmetry, entanglement, excitation, and topology, Adv. Phys. **64**, 519 (2015).

[8] T. Kurumaji, S. Seki, S. Ishiwata, H. Murakawa, Y. Kaneko, and Y. Tokura, Magnetoelectric responses induced by domain rearrangement and spin structural change in triangular-lattice helimagnets NiI_2 and CoI_2, Phys. Rev. B **87**, 014429 (2013).

[9] H. Liu, X. Wang, J. Wu, Y. Chen, J. Wan, R. Wen, J. Yang, Y. Liu, Z. Song, and L. Xie, Vapor deposition of magnetic van der Waals NiI_2 crystals, ACS Nano **14**, 10544 (2020).

[10] H. Ju, Y. Lee, K.-T. Kim, I. H. Choi, C. J. Roh, S. Son, P. Park, J. H. Kim, T. S. Jung, J. H. Kim, K. H. Kim, J.-G. Park, and J. S. Lee, Possible persistence of multiferroic order down to bilayer limit of van der Waals material NiI_2, Nano Lett. **21**, 5126 (2021).

[11] Q. Song, C. A. Occhialini, E. Ergecen, B. Ilyas, D. Amoroso, P. Barone, J. Kapeghian, K. Watanabe, T. Taniguchi, A. S. Botana, S. Picozzi, N. Gedik, and R. Comin, Evidence for a single-layer van der Waals multiferroic, Nature (London) **602**, 601 (2022).

[12] A. S. Botana and M. R. Norman, Electronic structure and magnetism of transition metal dihalides: Bulk to monolayer, Phys. Rev. Mater. **3**, 044001 (2019).

[13] M. Lu, Q. Yao, C. Xiao, C. Huang, and E. Kan, Mechanical, electronic, and magnetic properties of NiX_2 ($X =$ Cl, Br, I) layers, ACS Omega **4**, 5714 (2019).

[14] V. V. Kulish and W. Huang, Single-layer metal halides $MX2$ ($X =$ Cl, Br, I): Stability and tunable magnetism from first principles and Monte Carlo simulations, J. Mater. Chem. C **5**, 8734 (2017).

[15] A. O. Fumega and J. L. Lado, Microscopic origin of multiferroic order in monolayer NiI_2, 2D Mater. **9**, 025010 (2022).

[16] J. Sødequist and T. Olsen, Type II multiferroic order in two-dimensional transition metal halides from first principles spin-spiral calculations, 2D Mater. **10**, 035016 (2023).

[17] J. Y. Ni, X. Y. Li, D. Amoroso, X. He, J. S. Feng, E. J. Kan, S. Picozzi, and H. J. Xiang, Giant biquadratic exchange in 2D magnets and its role in stabilizing ferromagnetism of $NiCl_2$ monolayers, Phys. Rev. Lett. **127**, 247204 (2021).

[18] C. Xu, J. Feng, M. Kawamura, Y. Yamaji, Y. Nahas, S. Prokhorenko, Y. Qi, H. Xiang, and L. Bellaiche, Possible Kitaev quantum spin liquid state in 2D materials with $S = 3/2$, Phys. Rev. Lett. **124**, 087205 (2020).

[19] C. Xu, J. Feng, H. Xiang, and L. Bellaiche, Interplay between Kitaev interaction and single ion anisotropy in ferromagnetic CrI_3 and $CrGeTe_3$ monolayers, npj Comput. Mater. **4**, 57 (2018).

[20] N. Liu, S. Zhou, and J. Zhao, High-Curie-temperature ferromagnetism in bilayer CrI_3 on bulk semiconducting substrates, Phys. Rev. Mater. **4**, 094003 (2020).

[21] L. Wu, L. Zhou, X. Zhou, C. Wang, and W. Ji, In-plane epitaxy-strain-tuning intralayer and interlayer magnetic coupling in $CrSe_2$ and $CrTe_2$ monolayers and bilayers, Phys. Rev. B **106**, L081401 (2022).

[22] S. R. Kuindersma, J. P. Sanchez, and C. Haas, Magnetic and structural investigations on NiI_2 and CoI_2, Physica B+C (Amsterdam) **111**, 231 (1981).

[23] X. Li, C. Xu, B. Liu, X. Li, L. Bellaiche, and H. Xiang, Realistic spin model for multiferroic NiI_2, Phys. Rev. Lett. **131**, 036701 (2023).

[24] S. Paul, R. Torsi, J. A. Robinson, and K. Momeni, Effect of the substrate on MoS_2 monolayer morphology: An integrated computational and experimental study, ACS Appl. Mater. Interfaces **14**, 18835 (2022).

[25] M. Bonilla, S. Kolekar, Y. Ma, H. C. Diaz, V. Kalappattil, R. Das, T. Eggers, H. R. Gutierrez, M.-H. Phan, and M. Batzill, Strong room-temperature ferromagnetism in VSe_2 monolayers on van der Waals substrates, Nat. Nanotechnol. **13**, 289 (2018).

[26] H. Yu, Z. Yang, L. Du, J. Zhang, J. Shi, W. Chen, P. Chen, M. Liao, J. Zhao, J. Meng, G. Wang, J. Zhu, R. Yang, D. Shi, L. Gu, and G. Zhang, Precisely aligned monolayer MoS_2 epitaxially grown on h-BN basal plane, Small **13**, 1603005 (2017).

[27] B. Li, Z. Wan, C. Wang, P. Chen, B. Huang, X. Cheng, Q. Qian, J. Li, Z. W. Zhang, G. Z. Sun, B. Zhao, H. F. Ma, R. X. Wu, Z. M. Wei, Y. Liu, L. Liao, Y. Ye, Y. Huang, X. D. Xu, X. D. Duan *et al.*, Van der Waals epitaxial growth of air-stable $CrSe_2$ nanosheets with thickness-tunable magnetic order, Nat. Mater. **20**, 818 (2021).

[28] D. Amoroso, P. Barone, and S. Picozzi, Spontaneous skyrmionic lattice from anisotropic symmetric exchange in a Ni-halide monolayer, Nat. Commun. **11**, 5784 (2020).

[29] S. Wu, X. Chen, C. Hong, X. Hou, Z. Wang, Z. Sheng, Z. Sun, Y. Guo, and S. Wu, Layer thickness crossover of type-II multiferroic magnetism in NiI_2, arXiv:2307.10686.

[30] M.-P. Miao, N. Liu, W.-H. Zhang, D.-B. Wang, W. Ji, and Y.-S. Fu, Spin-resolved imaging of atomic-scale helimagnetism in monolayer NiI_2, arXiv:2309.16526.

[31] X.-S. Ni, D.-X. Yao, and K. Cao, In-plane strain tuning multiferroicity in monolayer van der Waals NiI_2, arXiv:2209.12392.

[32] M. Amini, A. O. Fumega, H. González-Herrero, V. Vaňo, S. Kezilebieke, J. L. Lado, and P. Liljeroth, Atomic-scale visualization of multiferroicity in monolayer NiI_2, Adv. Mater. **36**, 2311342 (2024).

[33] Q. Cui, J. Liang, B. Yang, Z. Wang, P. Li, P. Cui, and H. Yang, Giant enhancement of perpendicular magnetic anisotropy and induced quantum anomalous Hall effect in graphene/NiI_2 heterostructures via tuning the van der Waals interlayer distance, Phys. Rev. B **101**, 214439 (2020).

[34] M. Cococcioni and S. de Gironcoli, Linear response approach to the calculation of the effective interaction parameters in the LDA $+ U$ method, Phys. Rev. B **71**, 035105 (2005).

[35] S.-W. Cheong and M. Mostovoy, Multiferroics: a magnetic twist for ferroelectricity, Nat. Mater. **6**, 13 (2007).

[36] R. Fei, W. Kang, and L. Yang, Ferroelectricity and phase transitions in monolayer group-IV monochalcogenides, Phys. Rev. Lett. **117**, 097601 (2016).

[37] J. Gou, H. Bai, X. Zhang, Y. L. Huang, S. Duan, A. Ariando, S. A. Yang, L. Chen, Y. Lu, and A. T. S. Wee, Two-dimensional ferroelectricity in a single-element bismuth monolayer, Nature (London) **617**, 67 (2023).

[38] D. L. Bao, A. O'Hara, S. Du, and S. T. Pantelides, Tunable, ferroelectricity-inducing, spin-spiral magnetic ordering in monolayer FeOCl, Nano Lett. **22**, 3598 (2022).

[39] J.-J. Zhang, L. Lin, Y. Zhang, M. Wu, B. I. Yakobson, and S. Dong, Type-II multiferroic $Hf_2VC_2F_2$ MXene monolayer with high transition temperature, J. Am. Chem. Soc. **140**, 9768 (2018).

[40] B. Huang, G. Clark, E. Navarro-Moratalla, D. R. Klein, R. Cheng, K. L. Seyler, D. Zhong, E. Schmidgall, M. A. McGuire, and D. H. Cobden, Layer-dependent ferromagnetism in a van der Waals crystal down to the monolayer limit, Nature (London) **546**, 270 (2017).

[41] T. Okubo, S. Chung, and H. Kawamura, Multiple-q states and the skyrmion lattice of the triangular-lattice Heisenberg antiferromagnet under magnetic fields, Phys. Rev. Lett. **108**, 017206 (2012).

[42] P. E. Blöchl, Projector augmented-wave method, Phys. Rev. B **50**, 17953 (1994).

[43] G. Kresse and D. Joubert, From ultrasoft pseudopotentials to the projector augmented-wave method, Phys. Rev. B **59**, 1758 (1999).

[44] G. Kresse and J. Furthmüller, Efficient iterative schemes for *ab initio* total-energy calculations using a plane-wave basis set, Phys. Rev. B **54**, 11169 (1996).

[45] G. Kresse and J. Furthmüller, Efficiency of *ab-initio* total energy calculations for metals and semiconductors using a plane-wave basis set, Comput. Mater. Sci. **6**, 15 (1996).

[46] I. V. Solovyev, P. H. Dederichs, and V. I. Anisimov, Corrected atomic limit in the local-density approximation and the electronic structure of d impurities in Rb, Phys. Rev. B **50**, 16861 (1994).

[47] L. M. Sandratskii, Noncollinear magnetism in itinerant-electron systems: Theory and applications, Adv. Phys. **47**, 91 (1998).

[48] R. D. Kingsmith and D. Vanderbilt, Theory of polarization of crystalline solids, Phys. Rev. B **47**, 1651 (1993).

[49] G. Henkelman, B. P. Uberuaga, and H. Jónsson, A climbing image nudged elastic band method for finding saddle points and minimum energy paths, J. Chem. Phys. **113**, 9901 (2000).

[50] S. Grimme, Semiempirical GGA-type density functional constructed with a long-range dispersion correction, J. Comput. Chem. **27**, 1787 (2006).

[51] J. P. Perdew, K. Burke, and M. Ernzerhof, Generalized gradient approximation made simple, Phys. Rev. Lett. **77**, 3865 (1996).

[52] L. Shulenburger, A. D. Baczewski, Z. Zhu, J. Guan, and D. Tománek, The nature of the interlayer interaction in bulk and few-layer phosphorus, Nano Lett. **15**, 8170 (2015).